RESEARCH ARTICLE

Key Points:
- A simple and computationally efficient approach was developed for real-time flood inundation mapping
- The approach, called GeoFlood, combines nonlinear filtering, geodesic minimization principles, prior information from low-resolution products, and the Height Above Nearest Drainage
- With simple hydraulic assumptions and approximate roughness estimation, GeoFlood rapidly generates flood maps corresponding well with those of detailed local models

Correspondence to:
P. Passalacqua,
paola@austin.utexas.edu

GeoFlood: Large-Scale Flood Inundation Mapping Based on High-Resolution Terrain Analysis

Xing Zheng[1], David R. Maidment[1] (iD), David G. Tarboton[2] (iD), Yan Y. Liu[3], and Paola Passalacqua[1] (iD)

[1]Department of Civil, Architectural and Environmental Engineering and Center for Water and the Environment, University of Texas at Austin, Austin, TX, USA, [2]Department of Civil and Environmental Engineering, Utah State University, Logan, UT, USA, [3]National Center for Supercomputing Applications, University of Illinois at Urbana-Champaign, Urbana, IL, USA

Abstract Recent floods from intense storms in the southern United States and the unusually active 2017 Atlantic hurricane season have highlighted the need for real-time flood inundation mapping using high-resolution topography. High-resolution topographic data derived from lidar technology reveal unprecedented topographic details and are increasingly available, providing extremely valuable information for improving inundation mapping accuracy. The enrichment of terrain details from these data sets, however, also brings challenges to the application of many classic approaches designed for lower-resolution data. Advanced methods need to be developed to better use lidar-derived terrain data for inundation mapping. We present a new workflow, GeoFlood, for flood inundation mapping using high-resolution terrain inputs that is simple and computationally efficient, thus serving the needs of emergency responders to rapidly identify possibly flooded locations. First, GeoNet, a method for automatic channel network extraction from high-resolution topographic data, is modified to produce a low-density, high-fidelity river network. Then, a Height Above Nearest Drainage (HAND) raster is computed to quantify the elevation difference between each land surface cell and the stream bed cell to which it drains, using the network extracted from high-resolution terrain data. This HAND raster is then used to compute reach-average channel hydraulic parameters and synthetic stage-discharge rating curves. Inundation maps are generated from the HAND raster by obtaining a water depth for a given flood discharge from the synthetic rating curve. We evaluate our approach by applying it in the Onion Creek Watershed in Central Texas, comparing the inundation extent results to Federal Emergency Management Agency 100-yr floodplains obtained with detailed local hydraulic studies. We show that the inundation extent produced by GeoFlood overlaps with 60%~90% of the Federal Emergency Management Agency floodplain coverage demonstrating that it is able to capture the general inundation patterns and shows significant potential for informing real-time flood disaster preparedness and response.

Plain Language Summary Simple and computationally efficient flood inundation mapping methods are needed to take advantage of increasingly available high-resolution topography data. In this work, we present a new approach, called GeoFlood, for flood inundation mapping using high-resolution topographic data. This approach combines GeoNet, an advanced method for high-resolution terrain data analysis, and the Height Above Nearest Drainage. GeoFlood can rapidly convert real-time forecasted river flow conditions to corresponding flood maps. A case study in central Texas demonstrated that the flood maps generated with our approach capture the majority of the inundated extent reported by detailed Federal Emergency Management Agency flood studies. Our results show that GeoFlood is a valuable solution for rapid inundation mapping.

1. Introduction

Flooding is the most threatening natural disaster worldwide considering the fatalities and property damage it causes. It makes up to 40% of all natural disasters worldwide and causes about half of all natural hazard fatalities (Noji, 1991; Munich, 2015; Ohl & Tapsell, 2000). The unusually active 2017 Atlantic hurricane season was the costliest hurricane season in the North American record (Munich, 2018). Associated flood disasters have raised concerns for accurate and responsive inundation forecasts due to the rapid spread and astonishing destructive power of these events. In this work, we propose a novel approach, called GeoFlood, for approximate inundation mapping on high-resolution topographic data. Our approach couples the effective Height Above Nearest Drainage (HAND; Nobre et al., 2011, 2015) method and GeoNet, a channel extraction method designed for high-resolution lidar-derived terrain data (Passalacqua et al., 2010).

Inundation mapping captures the spatial extent of flooding and is one of the critical products used by first responders during a flood emergency response (Apel et al., 2009). Flood disasters caused by recent hurricanes Harvey, Irma, and Maria emphasized the need for rapid flood inundation mapping over very large areas. Inundation during and after hurricanes has various causes including storm surge, river flooding, and flash flooding. Among these flood mechanisms, river flooding is the focus of this manuscript.

Existing approaches to mapping inundation resulting from river flooding can be classified in three categories (Teng et al., 2017): empirical methods, hydrodynamic models, and simplified conceptual models. Empirical methods are based on observations (Schumann et al., 2009; Stephens et al., 2014) and can only provide guidance for real-time monitoring and postevent evaluation. Hydrodynamic models commonly create inundation maps by solving one-dimensional Saint-Venant equations or two-dimensional shallow water equations. Although these models can be parallelized to leverage a large amount of computing power and create continental-scale inundation maps at 30-m resolution or coarser (Dottori et al., 2016; Sampson et al., 2015; Schumann et al., 2013; Wing et al., 2017), running such models at higher resolutions or during real-time flood events remains computationally impractical. On the other hand, simplified geographic information system-based conceptual inundation mapping strategies have been developed (Zheng et al., 2018) and implemented at the continental scale at 10-m resolution (Liu et al., 2018). Efficient implementation on parallel computing platforms has accelerated classic hydrological terrain analyses, such as pit filling, flow direction, and flow accumulation area computation, from a monthly or daily task to an hourly task when performed at continental scale (Liu et al., 2018). Therefore, compared to the more physically rigorous but more computationally intensive hydrodynamic models, conceptual approaches are better prepared for emergency response by ingesting detailed inputs quickly because of their simplicity. Data-driven approaches without hydraulic assumptions have also been explored to evaluate flood risk in different regions; examples are advanced machine learning techniques such as artificial neural network (ANN; Kia et al., 2012; Ullah & Choudhury, 2013), frequency ratio (Lee et al., 2012), analytic hierarchy process (AHP; Matori et al., 2014; Siddayao et al., 2014), and fuzzy logic (Ullah & Choudhury, 2013). However, the general applicability of these approaches is still unknown, considering the need for multitype input features, the availability of existing results for model training, the requirement of experts' judgments, and the portability of the model parameters across different areas.

Previous research (Savage et al., 2015, 2016) suggested that inundation details derived from terrain information at fine spatial resolution may be unnecessary and cause overconfidence in the mapping outputs. In terms of modeling, there are also associated uncertainties in friction parameters and boundary conditions. However, the opportunities provided by high-resolution topographic data derived from advanced remote sensing technology such as light detection and ranging (lidar) are obvious (Bates, 2012; Casas et al., 2006; Hilldale & Raff, 2008; Passalacqua et al., 2015; Tarolli, 2014). This type of data is especially critical for inundation mapping in areas where artificial structures such as buildings and roads dominate flow patterns and may be undetectable in coarse terrain data sets (when the grid cell size is larger than the feature of interest). On the other hand, high-resolution terrain data introduce both highly detailed information and data uncertainties (e.g., errors) that may not exist in terrain data of coarse resolution and may significantly influence inundation mapping model assumptions, applicability, and results. For instance, artificial structures may need to be identified and processed to create a flow continuum (i.e., a burn-in process for appropriate flow direction detection) if a model assumes a flow continuum in a study area. Also, the discrepancies between the flow network derived from high-resolution digital elevation models (DEMs) and that in published flow network data sets of lower resolution (e.g., National Hydrography Dataset Plus) become more significant. Errors in lidar-derived DEMs such as voids and vertical errors may also need explicit handling for a study area of high horizontal resolution. While it has been suggested that higher spatial resolution improves the local prediction of water depth rather than the extent of inundation (Leskens et al., 2014; Savage et al., 2016), systematic quantitative comparisons between inundation maps created with different resolution terrain inputs have not been performed thus far over areas of different characteristics.

The main goal of this paper is to present a method, called GeoFlood, which is able to create high-resolution inundation maps at low computational cost. Our method uses a simplified conceptual inundation mapping approach (Zheng et al., 2018) and lidar-derived high-resolution topographic data, and it is based on the HAND method (Nobre et al., 2011, 2015). Liu et al. (2018) evaluated HAND over the continental United States using a 10-m DEM. One key output of this approach is a HAND raster that provides the elevation

difference between each land surface cell and the stream bed cell to which it drains. In a recently proposed approach (Zheng et al., 2018) this HAND raster is used to derive the channel geometric properties of each stream segment. A synthetic rating curve for each segment is then computed from these channel properties and then used to convert a flow time series into a corresponding water level time series. Inundation maps are then created for the water level at each time step from the HAND raster. In the approach of Zheng et al. (2018), a DEM-derived channel network is used as the local datum to evaluate the flood risk at any given location. The accuracy of the channel delineation may significantly affect the resulting inundation extent. Innovative approaches for automatic channel extraction from lidar data have been developed (e.g., Johansen et al., 2013; Orlandini et al., 2011; Passalacqua et al., 2010; Pelletier, 2013; Sangireddy et al., 2016), but these approaches have not been coupled with inundation mapping techniques. Here we further develop the approach of Zheng et al. (2018) for its application to high-resolution terrain data. To address formidable challenges of river network identification associated with high-resolution terrain data, we extract channel networks for HAND computation and inundation mapping by enhancing GeoNet (Passalacqua et al., 2010), a method for the automatic extraction of channel networks from lidar-derived DEMs. The GeoNet approach combines nonlinear multiscale filtering and geodesic least-cost-path search to handle data precision and uncertainty issues in high-resolution DEMs. The coupling of GeoNet and HAND creates GeoFlood, a novel approach for high-resolution inundation mapping.

When compared to observed flooding extent, detail hydraulic analyses are not error free due to the data and method limitations (Ward et al., 2017; Wood et al., 2016). However, they represent the most accessible and understandable inundation information for general end users and have been adopted in multiple flood hazard studies as benchmark (Sampson et al., 2015; Ward et al., 2017; Wing et al., 2017). Therefore, in this study we choose Federal Emergency Management Agency (FEMA) 100-yr flood maps to validate the inundation results generated from GeoFlood.

The paper is organized as follows: After introducing the study area (the Onion Creek watershed, Central Texas) and data preparation (section 2), we present how the GeoNet approach and the HAND approach are coupled (section 3) to extract an improved river network and create a complete inundation mapping workflow. To evaluate the performance of our coupled workflow, we create inundation maps for several streams in our test watershed, which flow through different landscape settings, under the 100-yr flood scenario defined by a FEMA flood insurance study. HAND-derived synthetic rating curves and inundation maps are compared with field observations and simulated outputs. We then examine possible reasons for the differences in the results (section 4) and examine the effect of roughness coefficient uncertainty (section 5). We conclude that our approach is able to capture the general inundation patterns and shows significant potential in guiding real-time flood disaster preparedness and response (section 6).

2. Study Area

The study area (Figure 1) is the Onion Creek watershed, a tributary watershed of 892 km^2 to the Colorado River. Morphologically, this watershed represents a typical rolling terrain transition from the eastern edge of the Edwards Plateau to the western edge of the Gulf Coastal Plain. A high-resolution bare-Earth DEM (3-m resolution) was generated by combining point clouds acquired in aerial collections during the leaf-off season of 2007, 2008, and 2012 covering different parts of the watershed. The complete DEM was provided by the Texas Natural Resources Information System. The elevation of this DEM ranges from 113 to 510 m above sea level with an average of 289 m. The slope varies from 0° to 77.3° with an average of 4°.

The area lies on the border between a subtropical humid climate and a subtropical subhumid climate with a mean annual rainfall of about 850 mm. Precipitation occurs mainly in late spring and early autumn. Flash flooding caused by short-term high-intense storms during these periods brings serious threats to life and property in this watershed. On 31 October 2013, a flood event resulted in 4 fatalities, 825 impacted homes, 40 closed roads, and more than $10 million in public infrastructure damage (Vigil et al., 2016). Flooding reached the highest recorded depth of 12.2 m since 1921 with an estimated discharge of 3,820 m^3/s (Vigil et al., 2016). Two years later, another storm was recorded over the same area on 30 October 2015, when 35 cm of precipitation fell on the Onion Creek watershed in 6 hr. Water level measurements at U.S. Geological Survey (USGS) gauge 08159000 reached 12 m with a peak discharge of 3,454 m^3/s (Vigil et al., 2016). The 2015 flood led to 3 fatalities and 400 damaged structures mainly located in the same area as
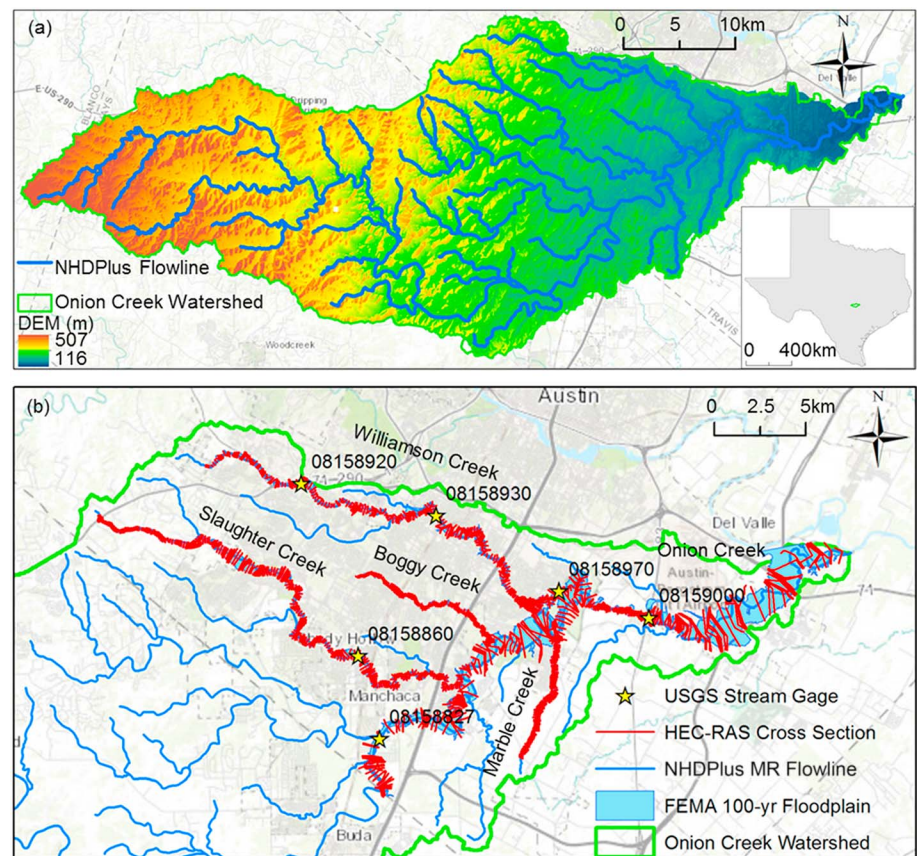
Figure 1. The Onion Creek Watershed study area. (a) Location map of the study area and NHDPlus MR network with 3-m DEM as background. The watershed outlet is located at 30°12′18″N, 97°35′24″W. (b) Lower portion of the watershed and cross sections on five streams from the local HEC-RAS model and FEMA 100-yr floodplain. DEM = digital elevation model; FEMA = Federal Emergency Management Agency; USGS = U.S. Geological Survey; NHDPlus MR = National Hydrography Dataset Plus Medium Resolution; HEC-RAS = Hydrologic Engineering Center's River Analysis System.

the 2013 flood. Frequent severe flooding disasters call for more comprehensive understanding of the flooding process in this watershed, providing practical reasons for choosing it as a test site.

Calibrated hydraulic models and inundation maps are available for the main stem river and major tributaries in the Onion Creek watershed. These models were created by local consulting companies and approved by the City of Austin and FEMA for flood mitigation purposes (FEMA, 2016). However, these inundation maps only simulate the scenarios corresponding to several given return period events such as the 100-yr flood (Figure 1b) and the 25-yr flood estimated with flood frequency analysis. Therefore, these maps cannot capture the complex dynamic characteristics of an extreme flood event, which may exceed the magnitude of the simulated scenarios. This limitation was confirmed by the impact estimation process after the 2015 flood, which concluded that extensive flooding occurred beyond the mapped floodplains (Vigil et al., 2016). The end products of the FEMA flood study are floodplain polygons. These features describe the spatial extent of flooding water in a more comprehensive way than the high water marks collected during historic flood events, which are sample points sparsely distributed over the domain of interest. For historic events, peak flow information is needed to derive the corresponding flood extent. This type of information is available only at a limited number of stream gauges. The FEMA study provides detailed discharge information corresponding to a given return period for several rivers and tributaries in the watershed of interest.

To evaluate the quality of the different components produced by our proposed workflow GeoFlood, we selected multiple standardized data sets available in the public domain as references: the National Hydrography Dataset Plus Medium Resolution (NHDPlus MR) to evaluate the extracted channel network, measured rating curves at six USGS stream gauges located on the test creeks to test the synthetic rating

curves, and the FEMA 100-yr floodplains on five streams in the Onion Creek watershed (Onion Creek, Slaughter Creek, Williamson Creek, Marble Creek, and Boggy Creek) to test the extent and depth of inundation computed with GeoFlood. These floodplains were generated from 1-D steady state Hydrologic Engineering Center's River Analysis System (HEC-RAS) models with flow conditions estimated from flood frequency analyses, field surveyed channel cross sections including artificial structures, and roughness coefficients estimated based on field surveyed channel conditions.

3. Methods

3.1. Automatic Channel Network Extraction

As first step of our GeoFlood workflow, we use GeoNet (Passalacqua et al., 2010; Sangireddy et al., 2016) to automatically extract the river network centerlines from lidar-derived terrain data sets. The first step performed in GeoNet is a nonlinear filtering operation (Perona & Malik, 1990) to smooth out terrain variability at scales smaller than the scale of interest, which acts as noise for the network extraction task. Following the filtering operation, we compute the geometric curvature κ on the filtered DEM, defined as the gradient of the elevation gradient normalized by its magnitude:

$$\kappa = \nabla \cdot (\nabla h / |\nabla h|), \tag{1}$$

where h indicates elevation.

Convergent features of the landscape with positive curvature above a threshold are identified as likely channelized zones and referred to as the skeleton. The curvature threshold is automatically detected from a quantile-quantile plot, which compares the statistical distribution of curvature to a normal distribution. The transition from hillslopes to valleys is identified at the deviation of the curvature distribution from a straight line (normal distribution) in the positive tail (Lashermes et al., 2007). An additional threshold, called the skeleton thinning parameter, is applied to further thin the set of likely channelized pixels identified with the curvature analysis. This thinning operation is able to exclude small convergent areas that are not part of the channel network (Passalacqua et al., 2010).

Local artificial structures (e.g., roads, bridges, and dams) present in the terrain may disrupt the skeleton. This issue is addressed by extracting channel centerlines with a geodesic minimization approach, which ensures the continuity of the extracted network. This approach uses a geodesic cost function (Passalacqua et al., 2010; 2012) defined as

$$\psi = \frac{1}{\alpha A + \beta \kappa + \gamma S} , \tag{2}$$

where α, β, and γ are constants used for dimensionality and to normalize the difference in order of magnitude of the accumulation (A), curvature (κ), and skeleton (S) terms. The river network comprises the least-cost paths connecting the channel heads to the watershed outlet.

The classic GeoNet workflow has two limitations when applied to inundation mapping. First, GeoNet automatically identifies channel heads as the upstream end points of the skeleton branches. As GeoNet extracts the network based on terrain convergence, those extracted paths may or may not carry water at all times, resulting in a network that may be denser than the perennial one. Furthermore, slope-based flow directions computed from the DEM are affected by the presence of artificial structures, because the terrain signal reports the elevation at the top of the structure (e.g., a bridge) unless the structure is manually removed (e.g., cells covering major roads in the 10-m National Elevation Dataset [NED]). The computed flow accumulation area may thus have errors, resulting in inaccuracies of the extracted network. We propose reducing the density of the extracted network by using the channel heads of the perennial rivers defined in the NHDPlus MR. The stream network of the NHDPlus MR with the continental U.S. coverage is derived from the 30-m-resolution NED using a classic slope-based approach with extensive manual corrections. Because the accuracy of the NHDPlus MR is limited by its input spatial resolution and the extraction method, it is not suitable for direct use in high-resolution hydrological terrain analyses, but it provides helpful information on the approximate location of the river centerline. We propose to use the NHDPlus MR river network to create a prior sample space of likely channelized pixels within which accurate flow paths can
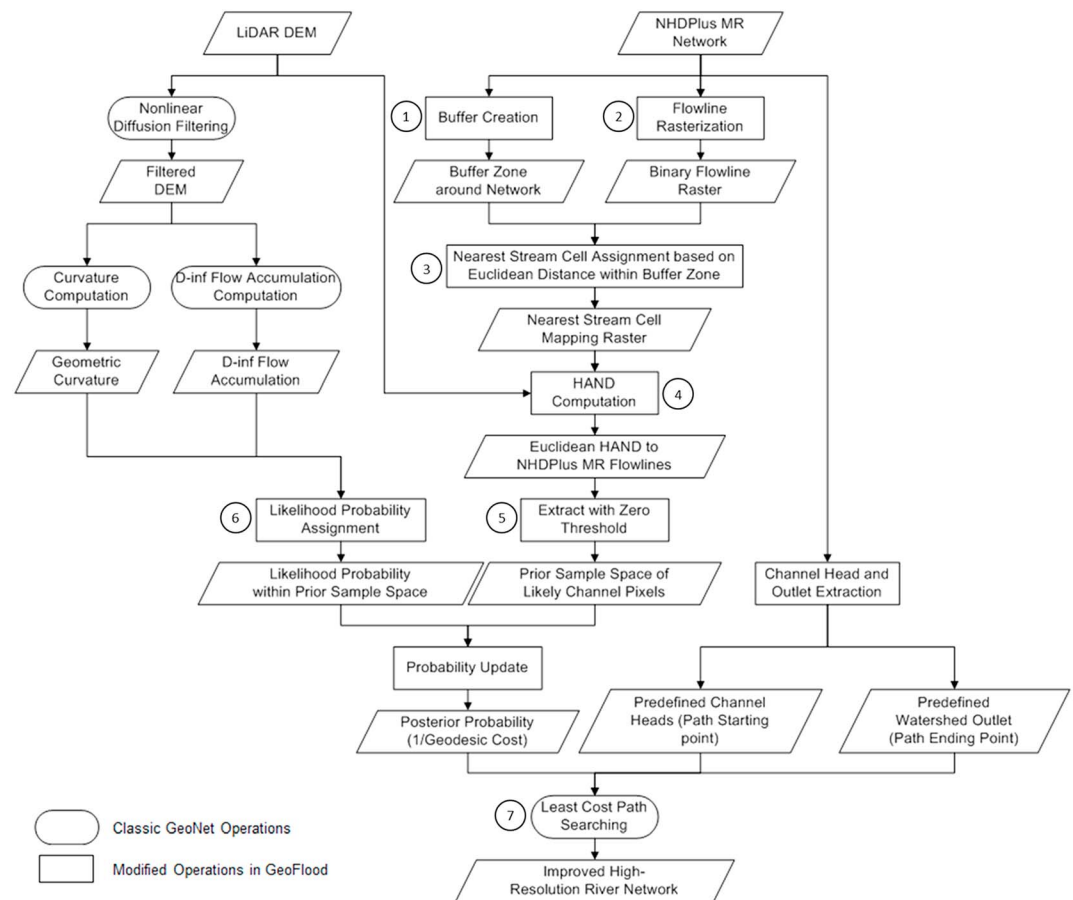
AGU
100
ADVANCING EARTH
AND SPACE SCIENCE

Water Resources Research

10.1029/2018WR023457

Figure 2. The channel network extraction workflow in GeoFlood. Existing GeoNet operations and new and modified operations are indicated by different box shapes. HAND = Height Above Nearest Drainage; NHDPlus MR = National Hydrography Dataset Plus Medium Resolution; DEM = digital elevation model.

be extracted, removing the inaccuracies introduced by topographic barriers and the coarser data resolution of the NHDPlus MR. We use the skeleton identified by GeoNet based on terrain curvature and flow accumulation as the likelihood function to update prior knowledge. We then develop a weighted geodesic minimization approach to obtain the posterior estimation of the river network.

The detailed steps of this weighted-geodesic-minimization extraction approach are as follows (Figure 2):

1. A buffer zone is created around the NHDPlus MR river network. The width of the buffer zone is set to be 10 times the maximum channel width at a given site.
2. The buffer zone is converted into a binary raster in which the value of 1 is assigned to all the cells that compose the flowlines (rasterized NHDPlus stream cells) and the value of 0 at all other cells.
3. For each cell within the buffer zone we identify its nearest stream cell based on Euclidean distance.
4. We compute the height difference between each cell and its nearest stream cell.
5. All the cells lower than the nearest stream cell form the prior sample space of likely channelized pixels. A high probability is assigned to all the cells within the prior sample space (0.99), and a low probability is assigned to all other cells (0.01). The assumption behind this operation is that if the NHDPlus MR flowline vertex is located on the thalweg, it will be retained, as the elevation of any other point along the transect will be higher. Otherwise, if the vertex is located outside the thalweg or outside the channel zone, only the cells that are lower than its elevation are considered part of the centerline.
6. Flow accumulation and curvature information are used to assign different likelihood probabilities to the cells in the prior sample space: If a pixel is part of the GeoNet skeleton (i.e., it has a large upstream contributing area and a positive curvature), it is very likely to be a centerline pixel. Therefore, its

likelihood probability is high (0.99). The probability of other pixels within the prior sample space is assigned equal to 0.01. The likelihood probability assignment forces the final network product to pass through as many skeleton pixels as possible. The posterior probability of each cell is updated as its prior probability times its likelihood probability.

7. We define the cost function as the reciprocal of the posterior probability. The river network is then extracted as a set of least-cost paths connecting the channel heads to their corresponding watershed outlet. Since the geodesic cost function depends on probability, the probability values assigned to the cells within (outside) the prior space and part of (outside) the skeleton will determine how closely the extracted network will follow the nonpositive relative height and skeleton criteria. Small changes to these probability values may lead to slight displacement of the extracted stream cell location, especially in correspondence of artificial structures, but will not modify substantially the extracted river network.

3.2. Channel Hydraulic Property and Rating Curve Estimation

Once the river network is extracted, a HAND raster is computed from the DEM as the relative height of each cell with respect to the nearest stream cell it drains to, determined using the D-infinity vertical distance to stream approach (Tesfa et al., 2011). Pits are filled in the DEM, and then D-infinity flow directions are computed (Tarboton, 1997). This flow direction grid is used, together with a stream raster constructed from the improved high-resolution river network from GeoNet to calculate the vertical distance from each grid cell to the streams, averaging across the multiple flow paths represented by the D-infinity flow model. At local depressions with elevation lower than the channel centerline datum, the elevation is filled during a pit-remove process to ensure connectivity to the stream pixels. However, the HAND value of these local depressions is computed from the raw DEM, thus may have a negative value, even though the flow directions are derived from a pit-filled DEM.

The approach recently reported by Zheng et al. (2018) is then followed to derive channel hydraulic properties and estimate rating curves from the HAND raster. We summarize the approach here for completeness. Given a centerline water depth h at a river segment, the HAND raster is used to produce a water depth grid of the inundated area $F(h)$ within the local catchment draining to that segment. The water depth d at any location i is computed as

$$d_i = \begin{cases} h - \mathrm{hand}_i, \text{if } \mathrm{hand}_i \leq h \text{ (flooded, } i \in F(h)), \\ 0, \text{if } \mathrm{hand}_i > h \text{ (not flooded, } i \notin F(h)). \end{cases} \tag{3}$$

Flood volume V, inundated surface area SA, and inundated bed area BA corresponding to the given depth are then derived from that depth grid:

$$\begin{aligned} V &= \Sigma_{i \in F(h)} d_i \cdot da_i, \\ SA &= \Sigma_{i \in F(h)} da_i, \\ BA &= \Sigma_{i \in F(h)} \sqrt{1 + s_i^2} \cdot da_i, \end{aligned} \tag{4}$$

where da_i is the cell area at location i and s_i is the planar slope computed with the D-inf algorithm at location i.

When the volume, surface area, and bed area are divided by the segment length L, the cross-sectional area, the channel top width, the wetted perimeter, and the hydraulic radius can be estimated for any water depth. Under the assumption of one-dimensional steady flow, the Manning's equation is then applied using the derived hydraulic properties to obtain a synthetic rating curve that links discharge Q and centerline water depth h, given the channel bed slope and the surface roughness coefficient.

To establish the aforementioned hydraulic properties for a river network, the extracted river centerlines are divided into segments (reaches) and the channel hydraulic properties are estimated separately for each segment. It is worth noting that if the reach length is too short, local terrain heterogeneity may cause variability of bed slope and other variables; on the other hand, if the reach length is too long, the hydraulic properties may bulk together too many channel geometry details, reducing the accuracy of the estimated hydraulic geometry characteristics on that reach. To avoid these problems, we divide river centerlines into 1.5-km-long segments in the current study.

Table 1
The Confusion Matrix

		FEMA hydrodynamic simulated inundation extent	
		Wet	Dry
GeoFlood inundation extent	Wet	True Wet (TW)	False Wet (FW)
	Dry	False Dry (FD)	True Dry (TD)

Note. FEMA = Federal Emergency Management Agency.

3.3. Inundation Mapping

As the last step of GeoFlood, a segment-based inundation mapping process is conducted using the HAND raster and the synthetic rating curves. During a flood event, a discharge time series is assigned to each segment in the network based on the results of hydrological simulations. From the discharge time series, we obtain the corresponding water depth time series using the synthetic rating curve. At each time step, the HAND value of any cell within the local catchment draining to the segment is compared to its real-time water depth estimation. If the HAND value is smaller than the depth, that cell is treated as inundated and the water depth at that cell is computed as the difference between the depth and the HAND value.

To evaluate the performance of the GeoFlood mapping results, two binary metrics, the fit index and the correct index, are calculated from the confusion matrix. These metrics treat the FEMA flood extent as benchmark and measure the performance of GeoFlood through operations such as intersection and union of the two inundation extents (Table 1):

The fit index (F) provides an overview of the method performance and accounts for overprediction and underprediction at the same time:

$$F = \frac{TW}{TW + FD + FW}. \tag{5}$$

The range of the F index varies from 0 (no overlap between two sets) to 1 (complete overlap).

The correct index (C) quantifies the percentage of the reference map inundation extent predicted:

$$C = \frac{TW}{TW + FD}. \tag{6}$$

This metric only evaluates a model's tendency toward underestimation and, therefore, is less strict than the fit index. The range of the C index also varies from 0 (no coverage) to 1 (complete coverage of the reference extent).

4. Results

To test the performance of GeoFlood, we implement it over the Onion Creek watershed. The NHDPlus MR flowlines extracted from a lower-resolution DEM are not able to accurately match the actual valley location as detected in the high-resolution terrain data set (see railway in Figure 3a). Also, artificial structures, for example, roads, are present in the topographic data set at this site, challenging the application of classic gradient-based channel extraction approaches (Figure 3a). As explained above, a negative height zone (relative to the NHDPlus MR flowline pixels) is identified based on the Euclidean distance (Figure 3b). This zone confines the likely channelized pixels within a smaller and uninterrupted domain. Curvature and flow accumulation are then used to assign likelihood probabilities to these pixels (Figure 3c). The new network extracted as the least-cost path from a given channel head to the outlet is more accurate than the original NHDPlus network (Figure 3d).

Once the stream network is extracted, the extracted centerline pixels are treated as the local datum used in the HAND calculation. A HAND raster is created from the raw 3-m DEM (Figure 4a). These centerlines are then divided into 1.5-km-long segments. The local drainage catchment is delineated for each segment and reach-average channel hydraulic parameters are derived for each river segment (Figure 4b) from the HAND subset within its local drainage catchment (Figure 5).

These hydraulic parameters are used in Manning's equation to derive a stage-discharge rating curve for each segment. Since all the rivers have been simulated with hydraulic models, the median Manning's n value of all intersecting cross sections is given by the reach-average value for a segment. If an USGS gauge measured rating curve is available, we compare our HAND-derived synthetic rating curve of the segment where the gauge is located to the field measurement.
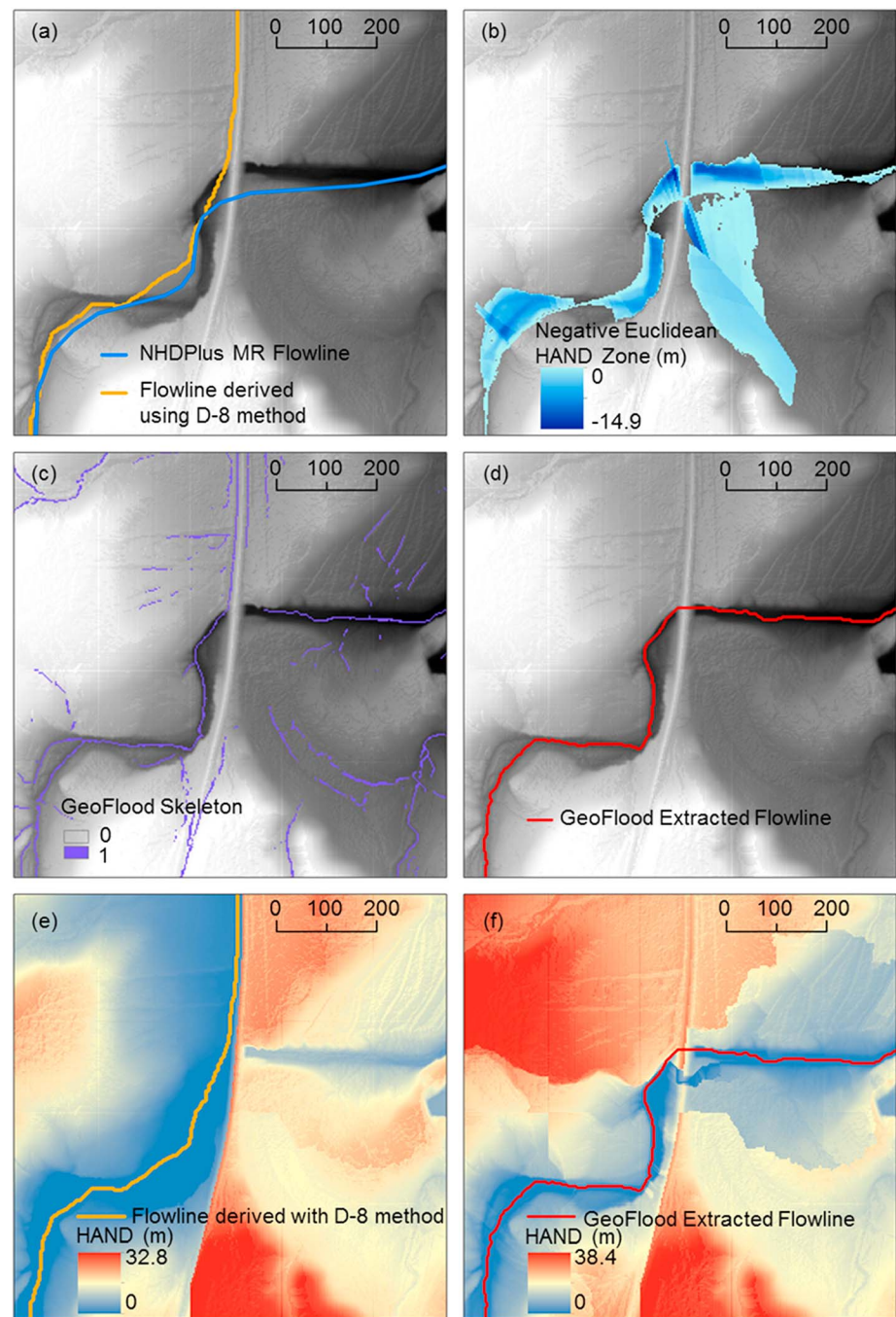
Figure 3. An example of the GeoFlood channel extraction method and the associated change in HAND values on a river crossing underneath a railway line: (a) Location of the original NHDPlus medium resolution flowline and the centerline extracted with the D-8 algorithm. (b) Negative HAND zone identified relative to the NHDPlus flowline based on Euclidean distance. (c) The skeleton of likely channelized pixels based on curvature and flow accumulation. (d) The geodesic least-cost path extracted as the final centerline product. (e) The HAND raster generated from lidar-derived digital elevation model relative to the D-8 centerline. (f) The HAND raster generated from lidar-derived digital elevation model relative to the improved centerline. NHDPlus = National Hydrography Dataset Plus; HAND = Height Above Nearest Drainage.

To quantitatively evaluate the performance of the HAND-derived rating curves, we compute the difference in water depths converted from the 100-yr flood discharge with two types of rating curves. If the 100-yr flood discharge is beyond the range of the gauge-measured rating curve, we use the 10-yr flood
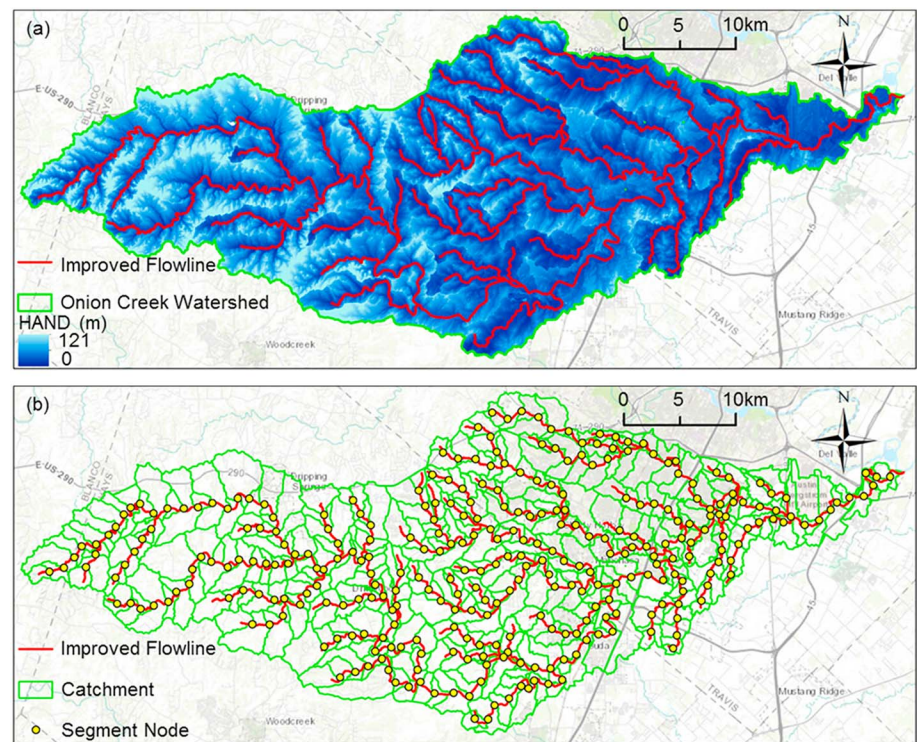
Figure 4. Hydrological terrain analysis products for the Onion Creek Watershed. (a) The improved river network extracted with the GeoFlood approach, overlaid with the 3-m HAND raster generated from the lidar-derived digital elevation model. (b) Constant-length segments along the network and local drainage catchment delineated for each segment. HAND = Height Above Nearest Drainage.

discharge instead. The flow conditions of given return periods are estimated from flood frequency analyses conducted by local model providers (FEMA, 2016).

The results (Figure 6 and Table 2) show that for the same magnitude flowrate of a given return period flood, the water depth converted from HAND-derived synthetic rating curves has an error of up to 30%. We find that the error tends to be larger on large rivers where the normal depth is deeper, compared to small tributaries. Two possible factors may account for this error: (i) the uncertainty of the roughness value applied in the
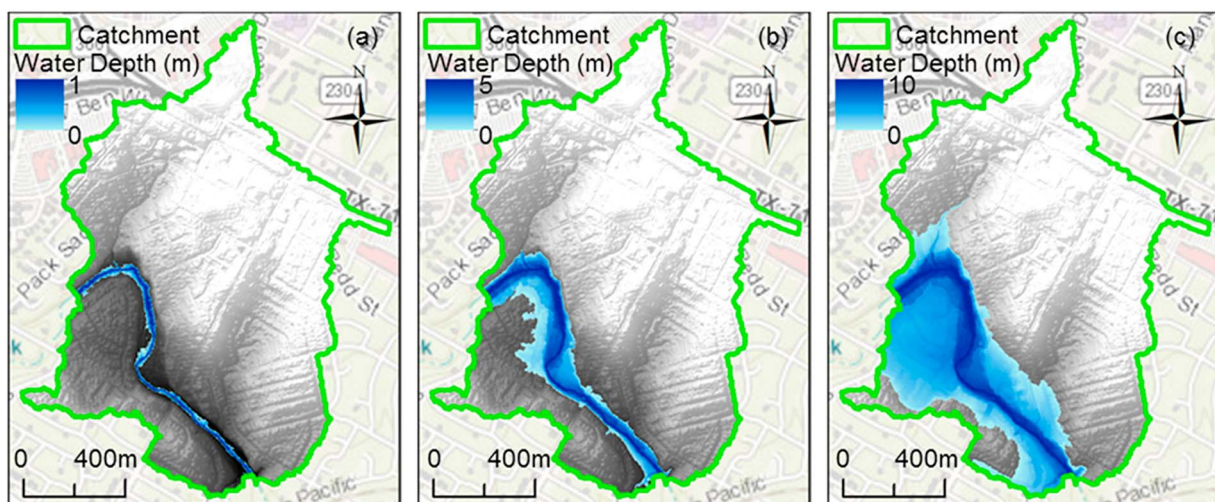

Figure 5. Example of GeoFlood inundation mapping derived from the Height Above Nearest Drainage raster corresponding to the 1-m (a), 5-m (b), and 10-m (c) water depths.
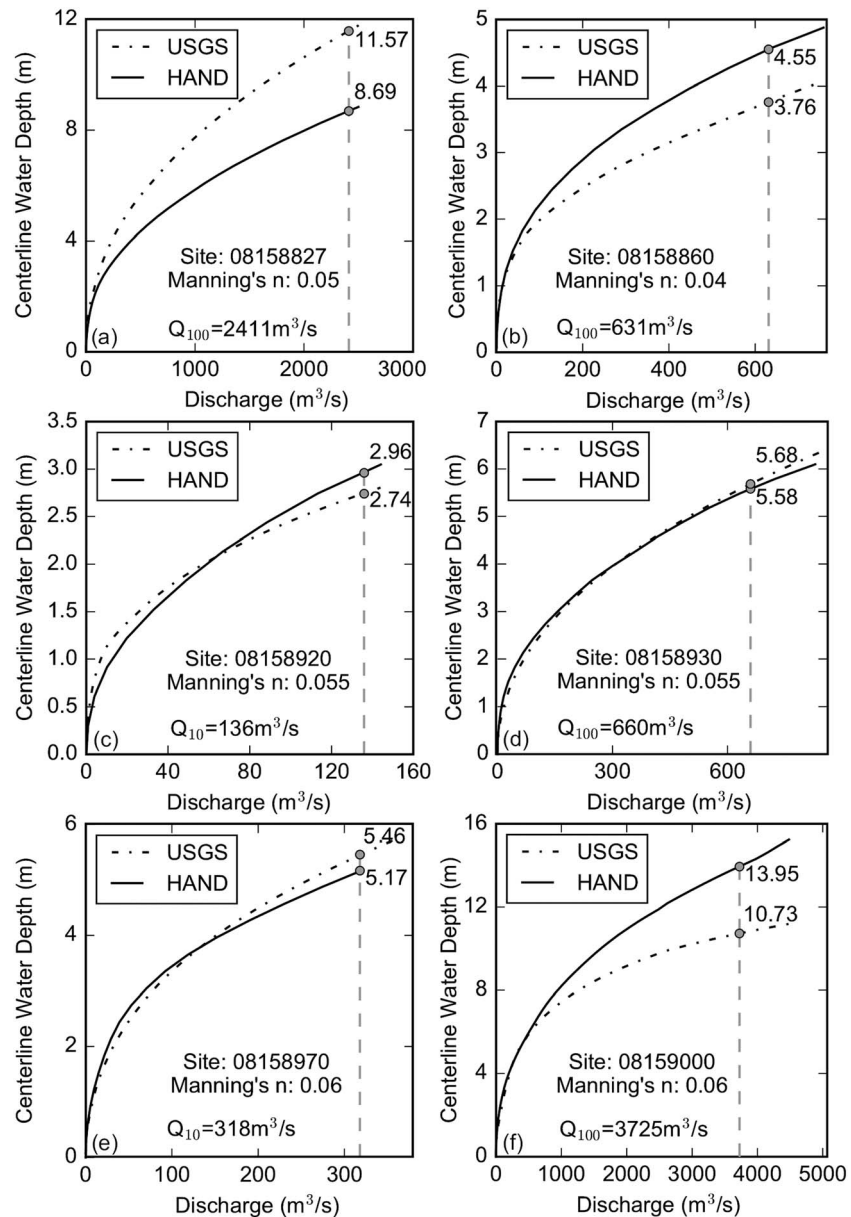
Figure 6. HAND-derived synthetic rating curve and USGS gauge-measured rating curve comparison at six USGS stream gauges in the Onion Creek watershed: (a) Onion Creek at Twin Creeks Road near Manchaca, TX; (b) Slaughter Creek at FM 2304 near Austin, TX; (c) Williamson Creek at Oak Hill, TX; (d) Williamson Creek at Manchaca Road, Austin, TX; (e) Williamson Creek at Jimmy Clay Road, Austin, TX; (f) Onion Creek at U.S. Highway 183, Austin, TX. HAND = Height Above Nearest Drainage; USGS = U.S. Geological Survey.

Manning's equation, which we discuss in a later section and (ii) the bathymetric information under normal flow condition, which is missing in lidar-derived terrain data sets (lidar data are mainly collected using a near-infrared (1,040–1,060 nm) laser beam, which has limited capability of penetrating water). Although the absence of bathymetric details in lidar data may lead to water depth underestimation, the effect on the final mapping accuracy may not be equivalently large, considering the limited portion of the total flood volume occupied by water in the channel during extreme flood events. We will return to this point later.

Acknowledging the uncertainties associated with the HAND-derived reach-average rating curves, we use these curves to convert the 100-yr-flood information from FEMA-approved HEC-RAS models into corresponding centerline water depths for each river segment. Within a single river segment, the centerline water depth is assigned as a constant value. The results show that across different segments, the depth varies

Table 2
Comparison of Water Depths Converted With HAND-Derived Synthetic Rating Curves and USGS Gage-Measured Rating Curves for Given Return Period Discharges

USGS stream gauge site ID	Discharge (m^3/s)	Return period (years)	Manning's n	Gauge measured water depth (m)	HAND-derived water depth (m)	Absolute error (m)	Relative error (%)
08158827	2,411	100	0.05	11.57	8.69	2.88	24.89
08158860	631	100	0.04	3.76	4.55	−0.79	−21.01
08158920	136	10	0.055	2.74	2.96	−0.22	−8.03
08158930	660	100	0.055	5.68	5.58	0.1	1.76
08158970	318	10	0.06	5.46	5.17	0.29	5.31
08159000	3,725	100	0.06	10.73	13.95	−3.22	−30.01

Note. HAND = Height Above Nearest Drainage; USGS = U.S. Geological Survey.

but the variation along a river is still within a reasonable range (Figure 7). A general increasing trend is observed in the predicted reach average water depth from upstream to downstream throughout multiple tested rivers. The HAND raster is then used to map the corresponding inundation zone of each catchment. The output inundation extent map is compared to the FEMA 100-yr inundation maps, which has been rasterized to the same resolution and extent as the lidar-derived DEM from the initial floodplain polygon vector. Only river segments covered by FEMA hydraulic simulations are considered in the comparison. The
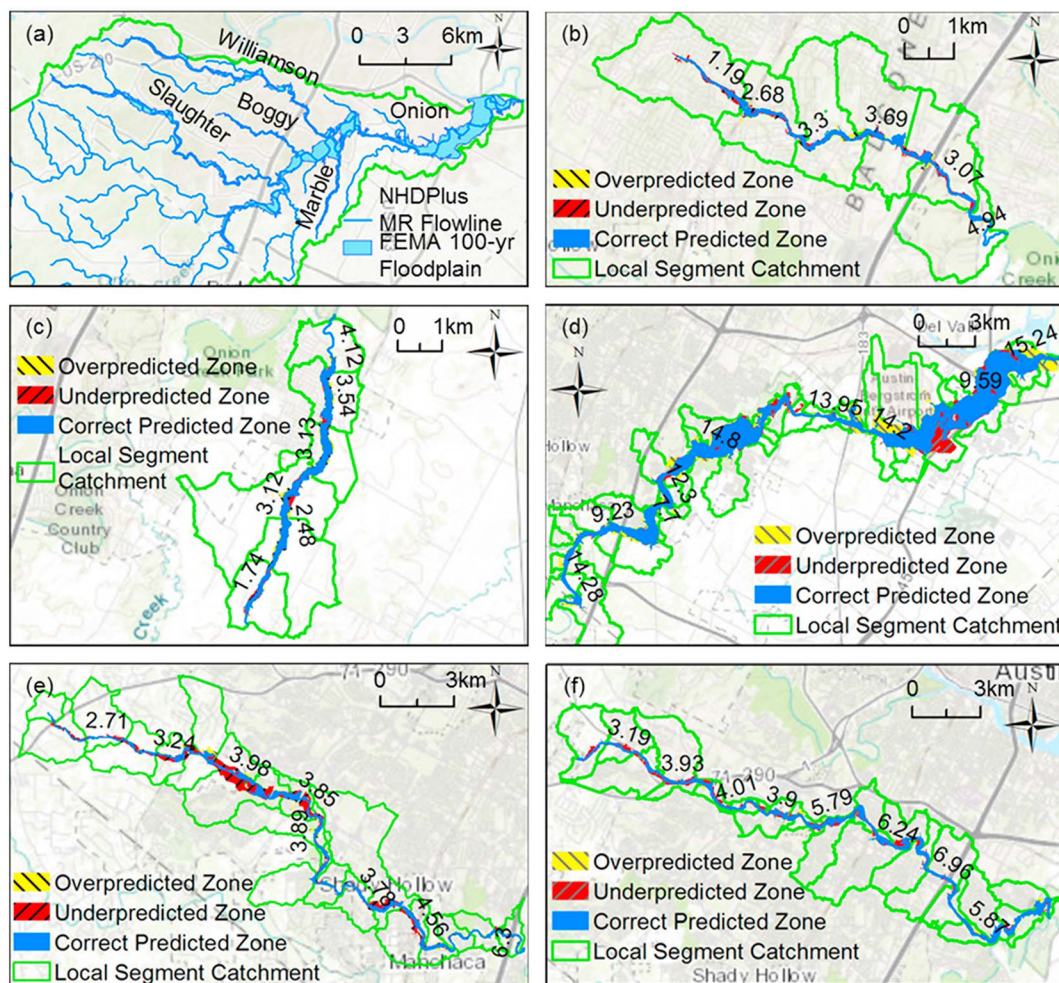

Figure 7. Comparison of HAND 100-yr inundation extent and FEMA 100-yr inundation layer on the whole watershed (a) and on Boggy Creek (b), Marble Creek (c), Onion Creek (d), Slaughter Creek (e), and Williamson Creek (f). (Numbers along the river indicate the reach-average water depth assigned to each river segment.) FEMA = Federal Emergency Management Agency; HAND = Height Above Nearest Drainage.

Table 3
Summary of HAND and FEMA 100-yr Inundation Extent Comparison

River	HAND inundation area ($\times 10^4$ m^2)	FEMA inundation area ($\times 10^4$ m^2)	Correct predicted area ($\times 10^4$ m^2)	Under predicted area ($\times 10^4$ m^2)	Over predicted area ($\times 10^4$ m^2)	F index	C index	Area ratio (HAND/FEMA)
Boggy Creek	56.59	63.96	49.42	14.54	7.17	0.69	0.77	0.88
Marble Creek	89.57	84.14	76.57	7.58	13.01	0.79	0.91	1.06
Onion Creek	2,088.44	1,931.83	1,697.20	234.63	391.24	0.73	0.88	1.08
Slaughter Creek	307.37	437.16	273.69	163.47	33.67	0.58	0.63	0.70
Williamson Creek	358.10	427.34	324.43	102.91	33.77	0.70	0.76	0.84

Note. FEMA = Federal Emergency Management Agency; HAND = Height Above Nearest Drainage.

results (Figure 7 and Table 3) show that the inundation extent computed by GeoFlood is able to capture the majority of the FEMA-simulated extent. When the inundation mapping performance metrics (Table 3) are computed by stream, the results show that the total flooded area computed by GeoFlood is close to that reported by the FEMA study. The *C* index values show that the GeoFlood extent overlaps 60%~90% of the FEMA floodplain coverage. When the GeoFlood area is plotted versus the FEMA-flooded area by local drainage catchment of each river segment (Figure 8), the points are approximately evenly distributed on the two sides of the diagonal line that indicates perfection estimation, suggesting that overall, the flood extent generated with the GeoFlood method is not larger nor smaller than the FEMA benchmark.

To better understand the improvement brought by the adoption of lidar-derived terrain inputs and the implementation of the equal-length segmentation in GeoFlood, we reproduce the inundation mapping results with two reference settings: In the first case, water depth and inundation extent are generated following the method described in section 3.3 using U.S. Geological Survey 1/3 arc sec (nominally 10 m) DEM and the original NHD network; in the second case, the same products are generated using U.S. Geological Survey 1/3 arc sec DEM and the equal-length-segment network. Compared to the initial NHDPlus network, the implementation of the equal-length segmentation results in more variation in water depth from upstream to downstream, but no significant change in water depth magnitude if the same DEM is used, while adopting lidar-derived topography results in water depths closer to the hydraulic simulation results (Figure 9). On Marble Creek, the root-mean-square error between the predicted water depth profile and the HEC-RAS-simulated one decreases from 0.99 m (NED and NHD network) to 0.77 m (NED and equal-length-segment network) to 0.59 m (lidar and equal-length-segment network). The performance metrics (Table 4) show that the adoption of lidar-derived topography does not lead to a significant improvement in inundation extent prediction at all the sites. For three of the five cases, the *F* index (0.69 > 0.59, 0.79 > 0.72, and 0.7 > 0.65) increases of 0.05 to 0.1. For the remaining two sites where a decrease in the *F* index is detected, the drop is relatively small (0.03). Therefore, based on our results, we conclude that lidar-derived high-resolution terrain inputs improve approximate inundation mapping in the prediction of both the water depth and the inundation extent. FEMA = Federal Emergency Management Agency; DEM = digital elevation model; NHD = National Hydrography Dataset; NED = National Elevation Dataset.

Figure 8. Comparison of the 100-yr inundation extent obtained with GeoFlood and by FEMA.

In terms of GeoFlood software and computing performance, we use the TauDEM (Tarboton, 2017; Wallis et al., 2009) and GeoNet (Passalacqua et al., 2010; Sangireddy et al., 2016) packages in combination with Environmental Systems Research Institute geoprocessing tools to perform the hydrological terrain analysis functions in the workflow. The most time demanding portion of the workflow is the channel network extraction, which for our study area takes 10 hr to execute on a single computational node with 68 Intel Xeon Phi 7250 cores and 96GB DDR4 RAM. For the generation of the HAND raster, the synthetic channel geometry and rating curves, and the inundation maps, TauDEM geoprocessing tools have been developed using a parallel computing framework (Zheng et al., 2018). These tools are executed with two computational nodes with 68 cores
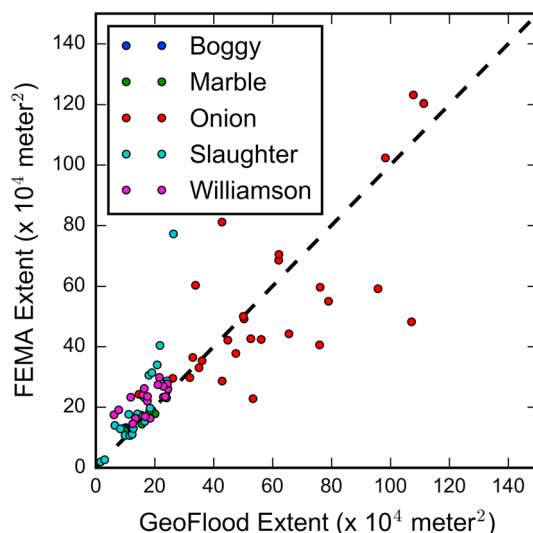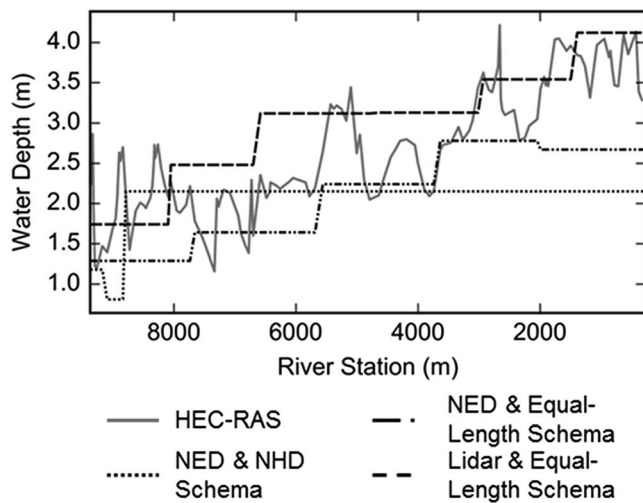
Figure 9. Comparison of 100-yr flood water depths predicted through synthetic rating curves using U.S. Geological Survey 1/3 arc sec NED, NHDPlus MR flowlines, U.S. Geological Survey 1/3 arc sec NED, equal-length NHDPlus MR stream segments, Texas Natural Resources Information System 3-m lidar-derived digital elevation model, equal-length improved stream segments with HEC-RAS-simulated water depth profile along Marble Creek. (River station represents distance to the stream outlet). NED = National Elevation Dataset; NHDPlus MR = National Hydrography Dataset Plus Medium Resolution.

on each node. The execution is completed within10 min. All the terrain analysis products have to be generated only the first time an area is analyzed. When the flow conditions change, the inundation mapping tool is run to create a new inundation map for the watershed, which for our study area takes less than 1 min.

5. Sensitivity Analysis: Effect of Roughness Coefficient and Terrain Characteristics

5.1. Manning's *n* Adopted in Rating Curve Derivation

The synthetic rating curves were derived with the Manning's *n* value used in local hydraulic models for each segment. The roughness coefficient (*n*) is determined by the type and size of riverbed materials, the character of the river, and the vegetation type and density. The coefficient estimated for individual cross sections, thus, may not reflect the average flow resistance of a river segment and large uncertainties exist in the coefficient estimation process. To further understand the effect of the roughness coefficient on the accuracy of the synthetic rating curves, we collected information on the possible Manning's *n* range for each river in the FEMA flood insurance study and tested the sensitivity of the water depth change associated with the change in Manning's *n*. The upper (computed with the minimum roughness coefficient) and lower (computed with the maximum roughness coefficient) dash line in each subplot of Figure 10 define the ensemble rating curve space. The dash dotted line represents the rating curve derived from USGS measurements. In all the cases, the measured rating curve falls within the ensemble rating curve space, indicating that the rating curve performance could be improved by adjusting the Manning's *n* value. Therefore, we tuned the *n* value in the given range to improve the water depth prediction corresponding to a given return period flow condition. After tuning the *n* value within a range, the synthetic rating curves are improved (shown as the solid lines in Figure 10) and are close to the USGS gauge measurements. We find that careful estimation of a reasonable roughness coefficient improves the accuracy of the predicted water depths.

In the current implementation of GeoFlood, a constant roughness coefficient is assigned to a given river segment without considering the resistance difference between the channel and the floodplain. Implementing a compound channel-floodplain roughness value is possible but requires an approach for identifying the location where roughness or geometric changes occur. We did not explore the compound approach here. However, it is a promising direction for future work that could improve the performance of HAND-derived synthetic rating curves.

5.2. Evaluation of Uncertainty Propagation From Rating Curves to Flood Extent

To better understand how the uncertainty in rating curves caused by the adoption of different Manning's *n* affects the accuracy of the inundation extent, we computed the inundation extent at different water levels, and the corresponding mapping metrics based on the comparison with the FEMA extents, and investigated how these metrics vary in the given water level range (Figure 11). The water level range is obtained by

Table 4

Summary of the 100-yr Inundation Extent Comparison Predicted by Federal Emergency Management Agency and GeoFlood With Different Terrain Inputs and Network Schemes

	Boggy Creek		Marble Creek		Onion Creek		Slaughter Creek		Williamson Creek	
	F Index	C Index	F Index	C Index	F Index	C Index	F Index	C Index	F Index	C Index
NED and NHDPlus MR	0.58	0.69	0.71	0.81	0.64	0.81	0.59	0.63	0.63	0.70
NED and Equal-length NHDPlus MR segments	0.59	0.70	0.72	0.82	0.76	0.90	0.61	0.67	0.65	0.76
Lidar and Equal-length Improved Flowline Segments	0.69	0.77	0.79	0.91	0.73	0.88	0.58	0.63	0.70	0.76

Note. NED = National Elevation Dataset; NHDPlus MR = National Hydrography Dataset Plus Medium Resolution.
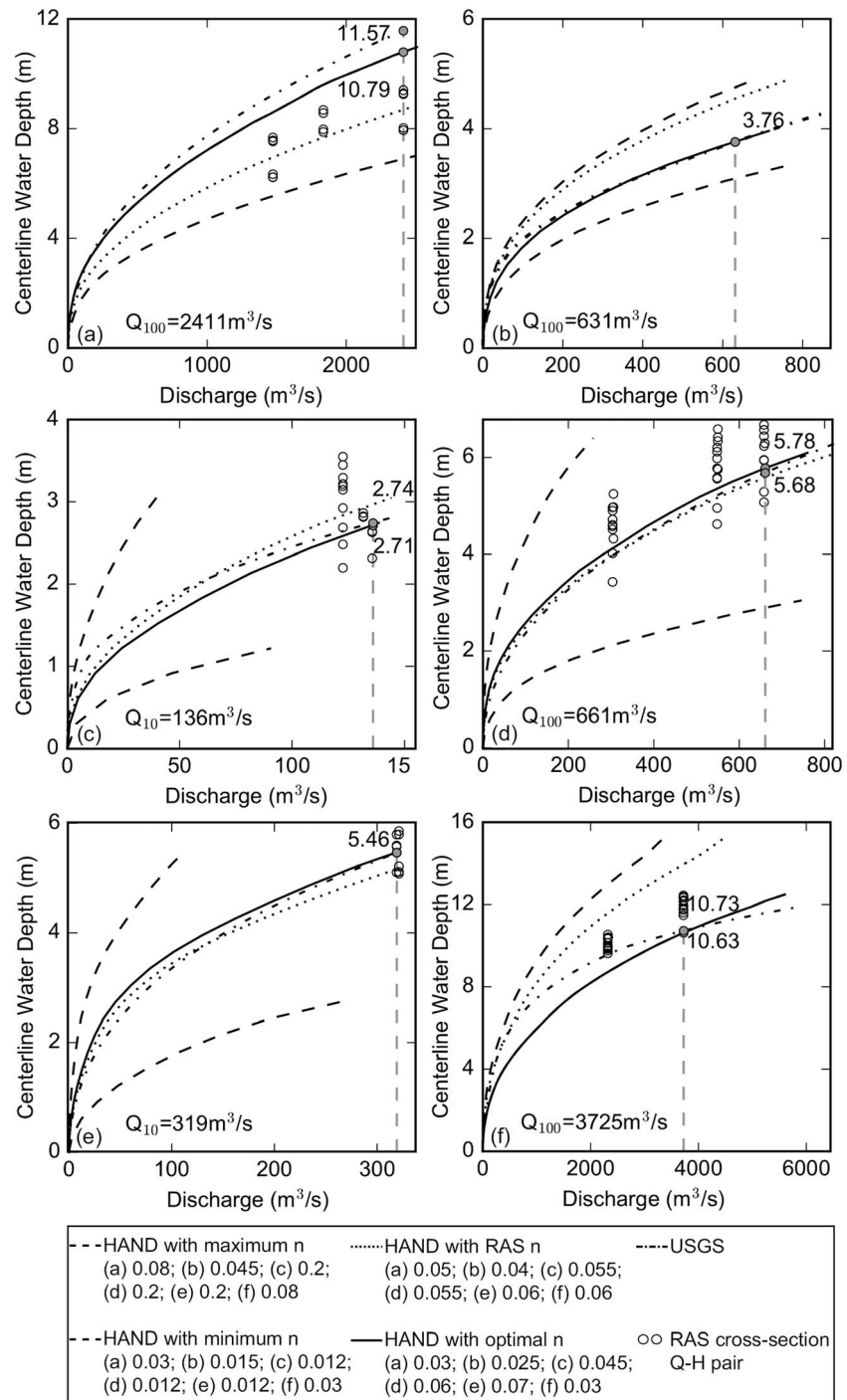
Figure 10. Roughness coefficient calibration for HAND-derived synthetic rating curve performance improvement with USGS gauge measured rating curves and HEC-RAS simulated flow-depth data pairs as reference: (a) Onion Creek at Twin Creeks Road near Manchaca, TX; (b) Slaughter Creek at FM 2304 near Austin, TX; (c) Williamson Creek at Oak Hill, TX; (d) Williamson Creek at Manchaca Road, Austin, TX; (e) Williamson Creek at Jimmy Clay Road, Austin, TX; (f) Onion Creek at U.S. Highway 183, Austin, TX. HAND = Height Above Nearest Drainage; USGS = U.S. Geological Survey.

converting the 100-yr flood discharge with the rating curves generated with the maximum and minimum Manning's n value for a given reach (Figure 10). GeoFlood results are compared to several water levels (Figure 11): the water depth predicted with synthetic rating curves with the roughness coefficient from HEC-RAS models ($H_{initial}$), the USGS-measured water depth corresponding to given flow conditions (H_{usgs}),
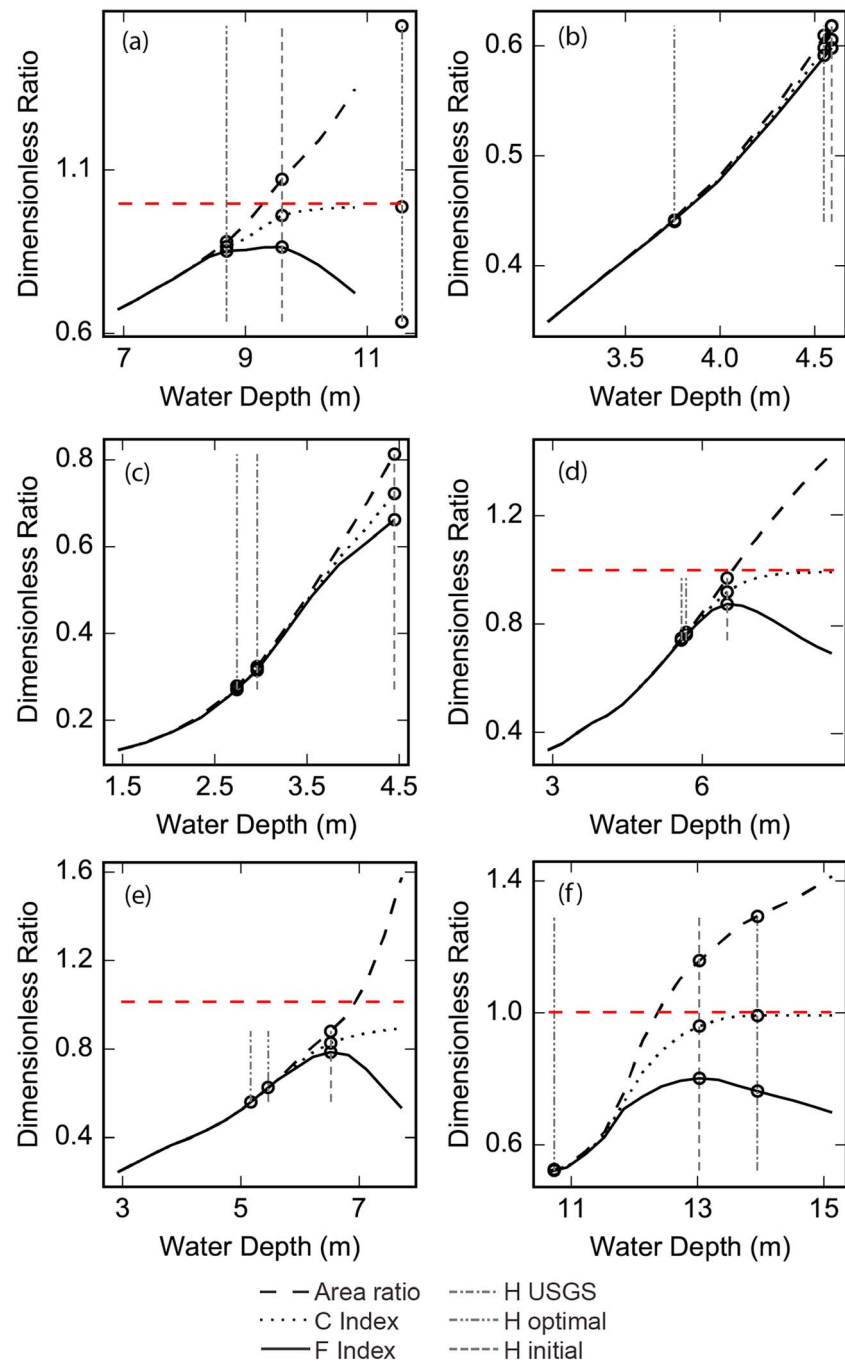
Figure 11. Change in the 100-yr inundation extent within the water depth range converted from rating curves with different Manning's *n* values: (a) Onion Creek at Twin Creeks Road near Manchaca, (b) Slaughter Creek at FM 2304 near Austin, (c) Williamson Creek at Oak Hill, (d) Williamson Creek at Manchaca Road, Austin, (e) Williamson Creek at Jimmy Clay Road, Austin, (f) Onion Creek at U.S. Highway 183, Austin. The plot range on the *x* axis is based on the centerline water depth range corresponding to the 100-yr flood discharge (Figure 10). The area ratio refers to the ratio of the area of the GeoFlood inundation extent to that of the Federal Emergency Management Agency 100-yr floodplain. USGS = U.S. Geological Survey.

and the water depth that returns the highest *F* index (best mapping performance; $H_{optimal}$). The results show that the most accurate water depth (USGS gauge measurements) does not necessarily result in the highest mapping accuracy. For some catchments (Figures 11b and 11c), the adjustment of Manning's *n* within a reasonable range does not ensure the best performance in terms of HAND flood extent, suggesting that
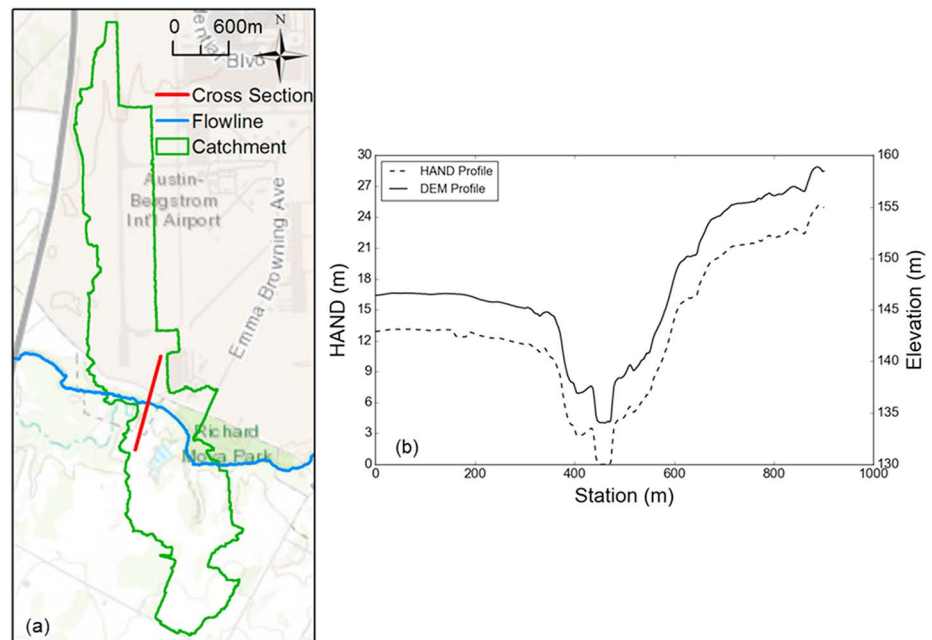
Figure 12. The location (a) and profile (b) of a cross section showing the different landscape setting on two sides of a river: a flat, urbanized terrain on the left-hand side and a hilly, natural terrain on the right-hand side.

additional modifications in the channel bed slope and river geometry estimation may be needed. At other sites, compared to the FEMA 100-yr floodplain, the highest F index of the GeoFlood extent reaches 0.79~0.87, which represents the upper limit of the proposed inundation mapping approach. The residual errors are due to the more complex hydrodynamic processes, which we are not able to capture with our approach based on terrain information only.

5.3. Analysis of Catchments With Lower Mapping Accuracy

We examine the limitations of GeoFlood in two catchments where the lowest mapping performance was reported. The first catchment analyzed is that draining to segment 237 in the Onion Creek watershed (Figure 12). This catchment has a unique topographic setting: the Austin International Airport is on the
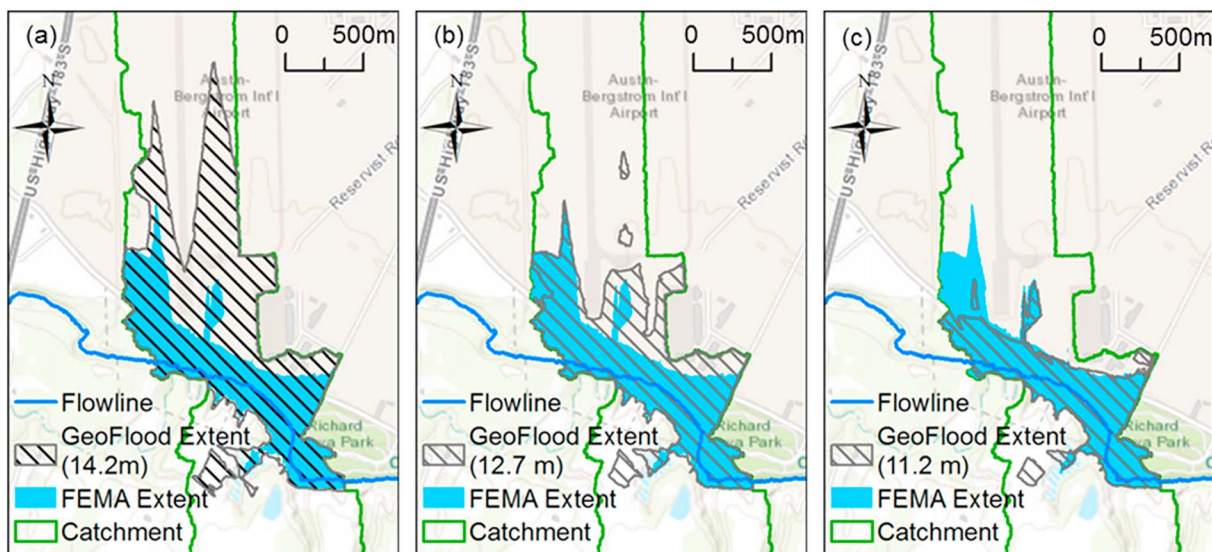

Figure 13. Inundation extents generated with GeoFlood corresponding to the 14.2-m (a), 12.7-m (b), and 11.2-m (c) water depths, showing how the sensitivity of mapping accuracy is affected by local topographic setting.
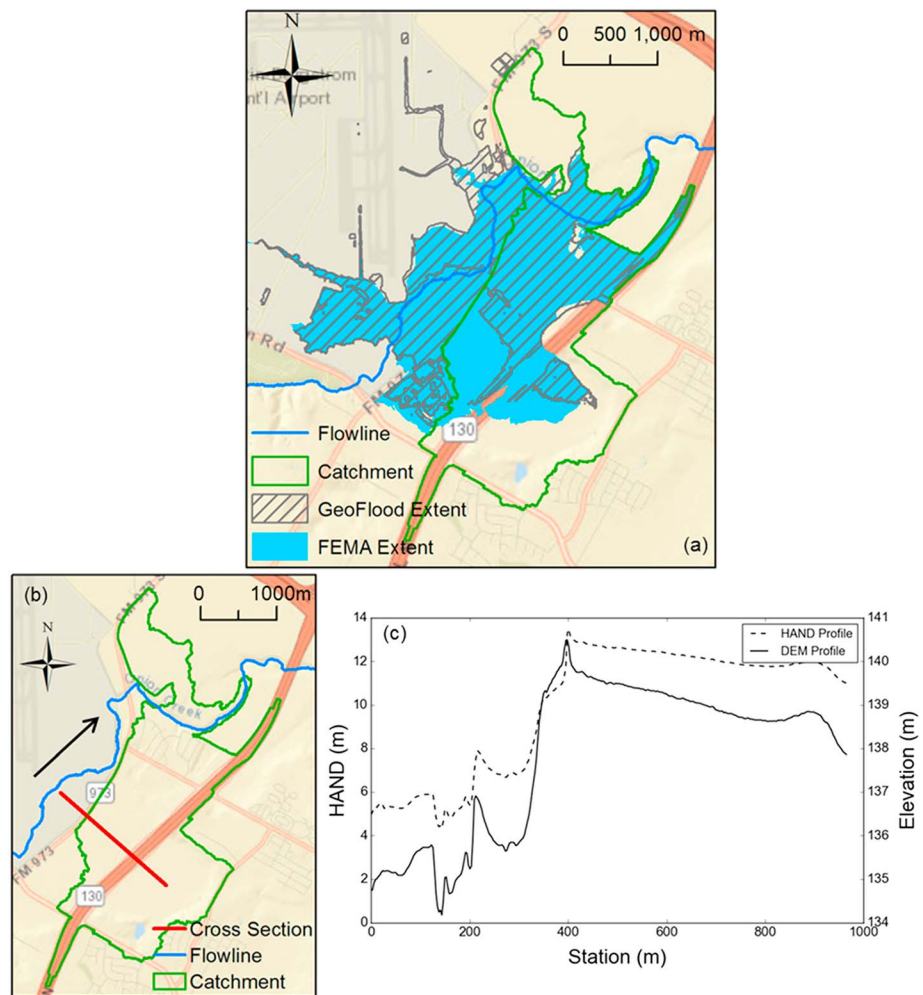
Figure 14. Underestimated GeoFlood inundation extents caused by the change of drainage pattern at different water levels. DEM = digital elevation model; HAND = Height Above Nearest Drainage.

left-hand side (upper) of the river, representing a typical urbanized flat area, while on the right-hand side (lower) is a natural hillside terrain. This difference can be easily seen in both the raw terrain data and the derived HAND product (Figure 12b).

The initial GeoFlood calculation for this catchment overestimates the flooding extent, compared to the FEMA 100-yr floodplain (Figure 13a). This initial extent was generated from the HAND raster using a threshold of 14.2 m, given by the 100-yr flow on the synthetic rating curves. In order to better match our inundation extent with the FEMA one, we identified the HAND values of the pixels on the edge of the FEMA floodplain and used these values to update the flooding extent. The extent corresponding to 12.7-m water depth was created to capture the sharp edge on the upper left corner (Figure 13b). Another extent corresponding to an 11.2-m water depth was created to capture the boundary on the right-hand side, which was also the average water depth computed from HEC-RAS for the cross sections intersecting with this river segment (Figure 13c). The results demonstrate that even with a significant change in water depth of 3 m, if the channel/floodplain is well shaped as in the natural landscape, the variation in flooding extent is relatively small; on the other hand, for flat, urbanized areas, the inundation extent obtained with the GeoFlood approach changes dramatically with small changes in water depth. This analysis demonstrates that our inundation mapping approach is more suitable as an approximate flood mapping strategy for a rural catchment as the one shown here. Also, local depressions such as ponds or waterbodies can be identified as flooded with GeoFlood even if they are not connected with the main stem river.
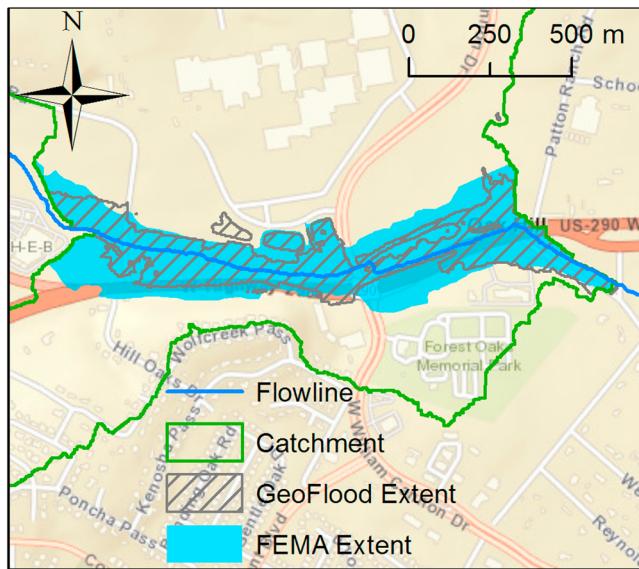
Figure 15. Underestimated GeoFlood inundation extents caused by the artificial structure elevation recorded in the digital elevation model. FEMA = Federal Emergency Management Agency.

To illustrate how the flow direction change associated with water depths affects the flood extent accuracy, we analyzed the second catchment corresponding to segment 254 on Onion Creek (Figure 14). Part of a local road (FM 973) is identified as the catchment boundary. On the east side of the catchment boundary road, the elevation drop in the raw DEM is larger than that in the HAND raster, as the stream segments chosen as the local datum for the HAND computation are different for two sides of the road: The closer upstream segment is the datum for the western side, and the further downstream segment is the datum for the eastern side. This choice results in relatively high HAND values for the eastern side pixels. However, the nearest drainage path at a given location can switch from one segment to another when the stage level exceeds the HAND value of the local catchment boundary. This change is not addressed by our current method as the nearest drainage relationship and the corresponding HAND values are always fixed for different water levels. Therefore, the flooded area near the catchment boundary is underestimated. In another case (Figure 15), the top elevation of a highway that passes through this catchment is detected by the lidar data, resulting in high HAND values for pixels where the highway bridge passes through. Therefore, the inundated area around the highway is also underestimated. This is a limitation of our approximate inundation mapping method due to the use of terrain information only. Detailed hydraulic models are able to account for artificial structures and may be necessary to depict a more accurate inundation extent in the proximity of these structures.

6. Conclusions

Fast-deployable, frequently updated, and high-resolution inundation mapping with broad coverage products are increasingly needed to support flood emergency preparation and response, calling for higher timeliness requirements to current mapping strategies. The increasing availability of high-resolution topography data over large areas makes their application in inundation mapping practice imperative. Additional challenges have to be addressed though including the high computational cost.

We presented a workflow, called GeoFlood, to address these challenges that relies on the application of the HAND method to lidar-derived high-resolution DEMs. Our proposed method extracts a high-fidelity network with a predefined network structure and density, derives reach-average channel hydraulic properties and stage-discharge rating curves for constant-length river segments in the network, and produces inundation maps for any segment of interest given the flood discharge. We presented a detailed analysis of a watershed in central Texas characterized by heterogeneous topography. We compared our rating curves to USGS gauge measurements and the inundation maps obtained with GeoFlood to those generated with detailed local hydraulic studies. Our results show that the inundation extent produced by our method overlaps with 60%~90% of the extent computed with hydraulic models. A sensitivity analysis shows that the accurate estimation of the roughness coefficient impacts the performance of the method in estimating accurate synthetic rating curves. The results indicate that our method performs better as an approximate inundation mapping method for fluvial flooding in hilly areas over large scales.

The novelty of GeoFlood lies in the adoption and enhancement of an advanced channel extraction approach, GeoNet, which is designed for analyzing high-resolution lidar-derived topographic data for inundation mapping. The original NHDPlus MR network, which is the foundation of continental-scale hydrologic simulation, was reorganized into constant-length segments to provide stable reach-average channel properties and synthetic rating curves. Our test results show that, given a sound estimation of the roughness coefficient, synthetic rating curves can approximate USGS gauge-measured stage-discharge relationships, which will be useful for hydrologic and hydraulic analyses in ungauged watersheds. While detailed terrain information is used in our inundation mapping strategy, its complexity and computational cost are still relatively low compared to fully physical hydrodynamic approaches, making it a promising tool for large-scale inundation mapping of high resolution.

The river network extraction, the HAND raster generation, and the synthetic channel geometry and rating curve computations in the workflow are one-time operations, which can be completed in hours. Once these products are ready, they can be used to create approximate inundation maps corresponding to different flood scenarios in minutes, greatly improving flood emergency response.

GeoFlood relies on large-scale hydrologic models to feed in real-time flow conditions. The uncertainty in these models will propagate to the predicted flood inundation extent. Probabilistic inundation maps derived from ensemble streamflow forecasts will better account for uncertainty than a deterministic inundation extent created from a flood scenario. The simplicity of GeoFlood in creating inundation extents and water depth grids at multiple stage levels makes it a promising flood mapping strategy to support such efforts in the future.

The application of GeoFlood requires an estimation of the channel roughness coefficient for each stream segment. Possible channel and floodplain roughness values for many U.S. rivers can be obtained from the FEMA flood insurance study report. For basins without available models, choosing a common value from the open channel Manning's roughness table is recommended based on knowledge about local channel type and condition. A previous study conducted by the authors (Zheng et al., 2018) has shown that applying this mapping strategy with a roughly estimated Manning's n value can still result in acceptable prediction of flood extent, although further calibration of the Manning's n can improve the results, as shown here.

Several aspects of the GeoFlood workflow can be improved: The currently adopted NHDPlus MR products could be replaced with the high-resolution NHDPlus products, which represent the best ground truth we have for hydrography at present, and could be used for prior probability definition and for the validation of extracted network. Proper segment lengths for different topographies should be estimated to obtain robust channel bed slopes, geometric properties, and rating curves. In the current study, the FEMA 100-yr floodplain was treated as the reference to check the integrity of the inundation mapping results because it is the most widely available and officially approved inundation product. However, significant uncertainties exist in FEMA 100-yr floodplains. Therefore, more tests should be conducted using ground truths collected during flood events, for example, USGS high water marks. Since the GeoFlood approach can also produce the water depth grid besides the inundation extent, further comparison between the GeoFlood depth grid and those generated with other methods such as hydrodynamic simulation is also recommended.

References

Apel, H., Aronica, G. T., Kreibich, H., & Thieken, A. H. (2009). Flood risk assessments—How detailed do we need to be? *Natural Hazards*, *49*(1), 79–98. https://doi.org/10.1007/s11069-008-9277-8

Bates, P. D. (2012). Integrating remote sensing data with flood inundation models: How far have we got? *Hydrological Processes*, *26*(16), 2515–2521. https://doi.org/10.1002/hyp.9374

Casas, A., Benito, G., Thorndycraft, V., & Rico, M. (2006). The topographic data source of digital terrain models as a key element in the accuracy of hydraulic flood modelling. *Earth Surface Processes and Landforms*, *31*(4), 444–456. https://doi.org/10.1002/esp.1278

Dottori, F., Salamon, P., Bianchi, A., Alfieri, L., Hirpa, F. A., & Feyen, L. (2016). Development and evaluation of a framework for global flood hazard mapping. *Advances in Water Resources*, *94*, 87–102. https://doi.org/10.1016/j.advwatres.2016.05.002

FEMA (2016). Flood insurance study: Travis County, Texas and incorporated areas. Retrieved from https://map 1.msc.fema.gov/data/48/S/PDF/48453CV001C.pdf? LOC=0562fb8b0786d89f646b85e5f2a9b2fc

Hilldale, R. C., & Raff, D. (2008). Assessing the ability of airborne LiDAR to map river bathymetry. *Earth Surface Processes and Landforms*, *33*(5), 773–783. https://doi.org/10.1002/esp.1575

Johansen, K., Grove, J., Denham, R., & Phinn, S. R. (2013). Assessing stream bank condition using airborne LiDAR and high spatial resolution image data in temperate semirural areas in Victoria, Australia. *Journal of Applied Remote Sensing*, *7*(1), 073492. https://doi.org/10.1117/1.JRS.7.073492

Kia, M. B., Pirasteh, S., Pradhan, B., Mahmud, A. R., Sulaiman, W. N. A., & Moradi, A. (2012). An artificial neural network model for flood simulation using GIS: Johor River Basin, Malaysia. *Environmental Earth Science*, *67*(1), 251–264. https://doi.org/10.1007/s12665-011-1504-z

Lashermes, B., Foufoula-Georgiou, E., & Dietrich, W. E. (2007). Channel network extraction from high resolution topography using wavelets. *Geophysical Research Letters*, *34*, L23S04. https://doi.org/10.1029/2007GL031140

Lee, M. J., Kang, J. E., & Jeon, S. (2012). Application of frequency ratio model and validation for predictive flooded area susceptibility mapping using GIS. In Geoscience and Remote Sensing Symposium (IGARSS), 2012 IEEE International. *IEEE*, 895–898. https://doi.org/10.1109/IGARSS.2012.6351414

Leskens, J. G., Brugnach, M., Hoekstra, A. Y., & Schuurmans, W. (2014). Why are decisions in flood disaster management so poorly supported by information from flood models? *Environmental Modelling & Software*, *53*, 53–61. https://doi.org/10.1016/j.envsoft.2013.11.003

Liu, Y. Y., Maidment, D. R., Tarboton, D. G., Zheng, X., & Wang, S. (2018). A CyberGIS Integration and Computation Framework for High-Resolution Continental-Scale Flood Inundation Mapping. *Journal of the American Water Resources Association*, *54*(4), 770–784.

Matori, A. N., Lawal, D. U., Yusof, K. W., Hashim, M. A., & Balogun, A. L. (2014). Spatial analytic hierarchy process model for flood forecasting: An integrated approach. *IOP Conference Series: Earth and Environmental Science*, *20*(1), 20–29. https://doi.org/10.1088/1755-1315/20/1/012029

Munich, R. E. (2015). *NatCatSERVICE loss events worldwide 1980–2014*. Munich: Munich Reinsurance.

Munich, R. E. (2018). *Topics 0 2017: Analyses, assessments, positions*. Munich: Munich Reinsurance Company.

Nobre, A. D., Cuartas, L. A., Hodnett, M., Rennó, C. D., Rodrigues, G., Silveira, A., et al. (2011). Height above the nearest drainage—A hydrologically relevant new terrain model. *Journal of Hydrology*, *404*(1-2), 13–29. https://doi.org/10.1016/j.jhydrol.2011.03.051

Nobre, A. D., Cuartas, L. A., Momo, M. R., Severo, D. L., Pinheiro, A., & Nobre, C. A. (2015). HAND contour: A new proxy predictor of inundation extent. *Hydrological Processes*, *30*(2), 320–333. https://doi.org/10.1002/hyp.10581

Noji, E. K. (1991). Natural disasters. *Critical Care Clinics*, *7*(2), 271–292. https://doi.org/10.1016/S0749-0704(18)30306-3

Ohl, C. A., & Tapsell, S. (2000). Flooding and human health: The dangers posed are not always obvious. *British Medical Journal*, *321*(7270), 1167–1168. https://doi.org/10.1136/bmj.321.7270.1167

Orlandini, S., Tarolli, P., Moretti, G., & Dalla Fontana, G. (2011). On the prediction of channel heads in a complex alpine terrain using gridded elevation data. *Water Resources Research*, *47*, W02538. https://doi.org/10.1029/2010WR009648

Passalacqua, P., Belmont, P., & Foufoula-Georgiou, E. (2012). Automatic geomorphic feature extraction from lidar in flat and engineered landscapes. *Water Resources Research*, *48*, W03528. https://doi.org/10.1029/2011WR010958

Passalacqua, P., Belmont, P., Staley, D. M., Simley, J. D., Arrowsmith, J. R., Bode, C. A., et al. (2015). Analyzing high resolution topography for advancing the understanding of mass and energy transfer through landscapes: A review. *Earth Science Reviews*, *148*, 174–193. https://doi.org/10.1016/j.earscirev.2015.05.012

Passalacqua, P., Trung, T. D., Foufoula-Georgiou, E., Sapiro, G., & Dietrich, W. E. (2010). A geometric framework for channel network extraction from lidar: Nonlinear diffusion and geodesic paths. *Journal of Geophysical Research*, *115*, F01002. https://doi.org/10.1029/2009JF001254

Pelletier, J. D. (2013). A robust, two-parameter method for the extraction of drainage networks from high-resolution digital elevation models (DEMs): Evaluation using synthetic and real-world DEMs. *Water Resources Research*, *49*, 75–89. https://doi.org/10.1029/2012WR012452

Perona, P., & Malik, J. (1990). Scale-space and edge detection using anisotropic diffusion. *IEEE Transactions on Pattern Analysis and Machine Intelligence*, *12*(7), 629–639. https://doi.org/10.1109/34.56205

Sampson, C. C., Smith, A. M., Bates, P. D., Neal, J. C., Alfieri, L., & Freer, J. E. (2015). A high-resolution global flood hazard model. *Water Resources Research*, *51*, 7358–7381. https://doi.org/10.1002/2015WR016954

Sangireddy, H., Stark, C. P., Kladzyk, A., & Passalacqua, P. (2016). GeoNet: An open source software for the automatic and objective extraction of channel heads, channel network, and channel morphology from high resolution topography data. *Environmental Modelling & Software*, *83*, 58–73. https://doi.org/10.1016/j.envsoft.2016.04.026

Savage, J. T. S., Bates, P., Freer, J., Neal, J., & Aronica, G. (2016). When does spatial resolution become spurious in probabilistic flood inundation predictions? *Hydrological Processes*, *30*(13), 2014–2032. https://doi.org/10.1002/hyp.10749

Savage, J. T. S., Pianosi, F., Bates, P. D., Freer, J., & Wagener, T. (2015). Quantifying the importance of spatial resolution and other factors through global sensitivity analysis of a flood inundation model. *Water Resources Research*, *52*, 9146–9163. https://doi.org/10.1002/2015WR018198

Schumann, G. J.-P., Di Baldassarre, G., & Bates, P. D. (2009). The utility of spaceborne radar to render flood inundation maps based on multi-algorithm ensembles. *IEEE Transactions on Geoscience and Remote Sensing*, *47*(8), 2801–2807. https://doi.org/10.1109/TGRS.2009.2017937

Schumann, G. J.-P., Neal, J. C., Voisin, N., Andreadis, K. M., Pappenberger, F., Phanthuwongpakdee, N., et al. (2013). A first large-scale flood inundation forecasting model. *Water Resources Research*, *49*, 6248–6257. https://doi.org/10.1002/wrcr.20521

Siddayao, G. P., Valdez, S. E., & Fernandez, P. L. (2014). Analytic hierarchy process (AHP) in spatial modeling for floodplain risk assessment. *International Journal of Machine Learning and Cybernetics*, *4*(5), 450–457. https://doi.org/10.7763/IJMLC.2014.V4.453

Stephens, E., Schumann, G., & Bates, P. D. (2014). Problems with binary pattern measures for flood model evaluation. *Hydrological Processes*, *28*(18), 4928–4937. https://doi.org/10.1002/hyp.9979

Tarboton, D. G. (1997). A new method for the determination of flow directions and upslope areas in grid digital elevation models. *Water Resources Research*, *33*(2), 309–319. https://doi.org/10.1029/96WR03137

Tarboton, D. G. (2017). Utah State University, TauDEM Web page. Retrieved from http://hydrology.usu.edu/taudem/taudem5

Tarolli, P. (2014). High-resolution topography for understanding Earth surface processes: Opportunities and challenges. *Geomorphology*, *216*, 295–312. https://doi.org/10.1016/j.geomorph.2014.03.008

Teng, J., Jakeman, A. J., Vaze, J., Croke, B. F. W., Dutta, D., & Kim, S. (2017). Flood inundation modelling: A review of methods, recent advances and uncertainty analysis. *Environmental Modelling & Software*, *90*, 201–216. https://doi.org/10.1016/j.envsoft.2017.01.006

Tesfa, T. K., Tarboton, D. G., Watson, D. W., Schreuders, K. A. T., Baker, M. E., & Wallace, R. M. (2011). Extraction of hydrological proximity measures from DEMs using parallel processing. *Environmental Modelling & Software*, *26*(12), 1696–1709. https://doi.org/10.1016/j.envsoft.2011.07.018

Ullah, N., & Choudhury, P. (2013). Flood flow modeling in a river system using adaptive neuro-fuzzy inference system. *Environmental Management and Sustainable Development*, *2*(2), 54–68. https://doi.org/10.5296/emsd.v2i2.3738

Vigil, M., Shunk, K., & McArthur, K. (2016). One creek, two floods: A comparison of the storms and response, TFMA 2016 Spring Conference, Houston, Texas, available online at <https://c.ymcdn.com/sites/www.tfma.org/resource/resmgr/SpringConference2016Presentations/Wed_5_One_Creek_Two_Floods.pdf>

Wallis, C., Wallace, R., Tarboton, D. G., Watson, D. W., Schreuders, K. A. T., & Tesfa, T. K. (2009). Hydrologic terrain processing using parallel computing. In R. S. Anderssen, R. D. Braddock, & L. T. H. Newham (Eds.), *18th World IMACS Congress and MODSIM09 International Congress on Modelling and Simulation* (pp. 2540–2545). Cairns, Australia: Modell. and Simul. Soc. of Aust. and N. Z. and Intl. Assoc. for Math. and Comput. in Simul.

Ward, P. J., Jongman, B., Aerts, J. C., Bates, P. D., Botzen, W. J., Loaiza, A. D., et al. (2017). A global framework for future costs and benefits of river-flood protection in urban areas. *Nature Climate Change*, *7*(9), 642. https://doi.org/10.1038/nclimate3350

Wing, O. E. J., Bates, P. D., Sampson, C. C., Smith, A. M., Johnson, K. A., & Erickson, T. A. (2017). Validation of a 30 m resolution flood hazard model of the conterminous United States. *Water Resources Research*, *53*, 7968–7986. https://doi.org/10.1002/2017WR020917

Wood, M., Hostache, R., Neal, J., Wagener, T., Giustarini, L., Chini, M., et al. (2016). Calibration of channel depth and friction parameters in the LISFLOOD-FP hydraulic model using medium-resolution SAR data and identifiability techniques. *Hydrology and Earth System Sciences*, *20*(12), 4983–4997. https://doi.org/10.5194/hess-20-4983-2016

Zheng, X., Tarboton, D. G., Maidment, D. R., Liu, Y. Y., & Passalacqua, P. (2018). River channel geometry and rating curve estimation using height above the nearest drainage. *Journal of the American Water Resources Association*, *54*(4), 785–806. https://doi.org/10.1111/1752-1688.12661

Erratum

In the originally published version of this article, equation 4 contained errors. It has been corrected, and this version may be considered the authoritative version of record.